Airborne measurements of spectral direct aerosol radiative forcing in INTEX/ITCT, 2004

Jens Redemann[1], Peter Pilewskie[2], Philip B. Russell[3], John M. Livingston[4], Steve Howard[1], Beat Schmid[1], John Pommier[1], Warren Gore[3], James Eilers[3], Manfred Wendisch[5]

[1]Bay Area Environmental Research Institute, Sonoma, CA

[2]University of Colorado, Boulder, CO

[3]NASA Ames Research Center, Moffett Field, CA

[4]SRI International, Menlo Park, CA

[5]Leibniz-Institute for Tropospheric Research, Leipzig, Germany

Submitted 10/24/05

Abstract

As part of the INTEX-NA (INtercontinental chemical Transport EXperiment-North America) and ITCT (Intercontinental Transport and Chemical Transformation of anthropogenic pollution) field studies, the NASA Ames 14-channel Airborne Tracking Sunphotometer (AATS-14) and a pair of Solar Spectral Flux Radiometers (SSFR) took measurements from aboard a Sky Research Jetstream 31 (J31) aircraft during 19 science flights (~53 flight hours) over the Gulf of Maine during 12 July – 8 August 2004. The combination of coincident and simultaneous AATS-14 and SSFR measurements yields plots of net (downwelling minus upwelling) spectral irradiance as a function of aerosol optical depth (AOD) as measured along horizontal flight legs. By definition, the slope of these plots yields the instantaneous change in net irradiance per unit AOD change and is referred to as the instantaneous spectral aerosol radiative forcing efficiency, E_i, [W m^{-2} nm^{-1}] at the surface. Numerical integration of the irradiance measurements over a given spectral range yields the instantaneous broadband aerosol radiative forcing efficiency [W m^{-2}]. This technique for deriving E_i is called the aerosol gradient method. In INTEX/ITCT, we observed a total of 14 horizontal AOD gradients, with 10 gradients well suited for our analysis because of the small changes in solar zenith angle during the gradient measurements. Within the 10 case studies we found a high variability in the derived instantaneous aerosol forcing efficiencies (forcing per unit optical depth) for the visible wavelength range (350-700 nm), with a mean of -79.6 W m^{-2} and a standard deviation of 21.8 W m^{-2}(27%). The mean instantaneous forcing efficiency for the visible plus near-IR wavelength range (350-1670 nm) was derived to be -135.3 W m^{-2} with a standard deviation of 36.0 W m^{-2} (27%). An analytical conversion of the instantaneous forcing efficiencies to 24h-average values yielded -45.8±13.1 W m^{-2} (mean±std)

for the visible and -82.9±23.1 W m^{-2} (mean±std) for the visible plus near-IR wavelength range, respectively. We present spectrally resolved aerosol forcing efficiencies between 350 and 1670 nm, estimates of the midvisible aerosol single scattering albedo and a comparison of observed broadband forcing efficiencies to previously reported values.

1 Introduction and definition of aerosol radiative forcing of climate

Atmospheric aerosols exert a direct effect on the Earth's radiation balance by scattering and absorbing solar and longwave radiation and an indirect effect through the modification of cloud radiative properties, as well as cloud formation and maintenance. Both effects can be studied using in situ [e.g., *Redemann et al*., 2000; *Fiebig et al*., 2002], satellite [e.g., *Zhang et al*., 2005; *Coakley et al*., 2002] or suborbital remote sensing data [e.g., *Hignett et al*., 1999; *Russell et al*., 1999; *Kim et al*., 2005], with advantages and drawbacks to each method. For the study of aerosol–climate interactions, we are mainly interested in aerosol effects on the atmospheric radiation balance. Hence, an actual measurement of atmospheric irradiance is preferable to methods which require the deduction of the aerosol effect on irradiance based on in situ aerosol properties or measurements of satellite radiances.

In this paper we use coincident airborne measurements of aerosol optical depth (AOD) and spectral solar irradiance to quantify the aerosol direct radiative effect, also referred to as the "aerosol direct radiative forcing of climate", hereafter denoted ΔF. There have been a number of different definitions and interpretations of this term. In most studies, aerosol radiative forcing of climate denotes the difference in net (downwelling minus upwelling) irradiance with and without

aerosols present. Direct aerosol radiative forcing is more clearly specified by adding terms to describe (i) the spectral range (e.g., visible, solar, shortwave, longwave), (ii) the time period (e.g., instantaneous, noon-time, diurnal average, "since pre-industrial times"), and (iii) the location within the atmosphere (e.g., surface, TOA- top of the atmosphere, TOL – top of the aerosol layer) for which the forcing is determined. These definitions are necessitated by the fact that ΔF is a strong function of wavelength, solar zenith angle, surface albedo, altitude of the aerosol layer, as well as atmospheric composition and aerosol optical properties [e.g., *Hansen et al*., 1997]. To match the aerosol radiative forcing to the corresponding aerosol change, the term aerosol radiative forcing efficiency, $E = \Delta F / \Delta \tau$, is introduced. It denotes the aerosol direct radiative forcing per aerosol optical depth change, the latter usually specified at midvisible wavelengths. The lack of or incomplete reporting of specific conditions has caused a great deal of confusion and misinterpretation of aerosol radiative forcing results in the literature.

Because aerosol radiative forcing of climate is defined as the difference in net iradiance with and without aerosols present, a measurement of this quantity is difficult to achieve. The most common method of deriving aerosol radiative forcing has been to measure net irradiance in the presence of aerosol, modeling net irradiance in the absence of aerosols and determining aerosol radiative forcing as the difference of the two. Here, we are primarily concerned with assessing the direct, solar (i.e., between 350 and 1700nm) aerosol radiative forcing efficiency, E_i and E_{24h}, with the subscripts "i" and "24h" denoting the instantaneous and the diurnally averaged values, respectively. All forcings and forcing efficiencies reported in this paper are measured near the surface at an altitude at or below 80 m above sea level (ASL) and determined from simultaneous,

low-level aircraft measurements of aerosol optical depth and net irradiance in aerosol optical depth gradients over dark water in the Gulf of Maine in the summer of 2004. This method has been termed the "aerosol gradient method" and was first proposed by *Pope and Valero* [2004] for airborne measurements collected in ACE-Asia (Aerosol Characterization Experiment – Asia) and INDOEX (Indian Ocean Experiment). With the exception of a model-based correction for changes in irradiance caused by changes in the solar zenith angle during the gradient observation period, the gradient method is an observationally-based assessment of aerosol direct radiative effects. The spectral range of the various results will be given in parentheses.

2 Measurements

In this paper we describe measurements aboard a Sky Research Jetstream 31 (J31) aircraft during 19 science flights (~53 flight hours) over the Gulf of Maine during 12 July – 8 August 2004 as part of the the INTEX-NA (INtercontinental chemical Transport EXperiment-North America) and ITCT (Intercontinental Transport and Chemical Transformation of anthropogenic pollution) field studies. The J31 was one of the platforms designated by ICARTT (International Consortium for Atmospheric Research on Transport and Transformation) to study the impact of aerosols on the atmospheric radiation balance. The observations important to this paper are spectral solar irradiance measured by a pair (nadir and zenith viewing) of spectral solar flux radiometers (SSFR) [e.g., *Pilewskie et al*., 2003] and spectral aerosol optical depth measured by the NASA Ames Airborne Tracking Sunphotometer (AATS-14) [e.g., *Russell et al*., 1999, *Redemann et al*., 2005].

The SSFR is used to simultaneously measure upwelling and downwelling irradiance between 350 and 1670 nm with a spectral resolution of 8-10 nm at a data rate of 1 Hz. Prior to and following field deployment the SSFR was calibrated using 1000 W NIST traceable irradiance standards. In the field a LI-COR Field Calibrator was used to monitor the stability of the SSFR over the duration of the experiment. The absolute accuracy of SSFR irradiance spectra is estimated to be 3-5% across the spectrum, while precision is between 0.1-0.5%. Because the derivation of forcing efficiency depends on the change in irradiance rather than its absolute magnitude the SSFR precision is more important than absolute accuracy. The greatest SSFR irradiance contribution to uncertainty in forcing efficiency comes from the aircraft attitude (discussed in Section 4.1).

AATS-14 measures direct solar beam transmission at 14 wavelengths between 354 and 2139 nm in narrow channels with bandwidths between 2 and 5.6 nm for the wavelengths between 354 and 1640 nm and 17.3 nm for the 2139 nm channel. The transmission measurements at all channels except 940 nm are then used to retrieve spectra of aerosol optical depth. In addition, the transmission at 940 nm is used to derive columnar water vapor [*Schmid et al*., 2001]. Radiometric calibration of AATS-14 is determined using the Langley-plot technique [cf., *Schmid and Wehrli*, 1995]; methods for AATS-14 data reduction, calibration, and error analysis have been described previously [*Russell et al*., 1993; *Schmid et al*., 1997 and 2001]. AATS-14 was calibrated based on pre-mission measurements at Mauna Loa Observatory in June 2004 and airborne Langley plots towards the end of the INTEX/ITCT experiment (i.e., late July-early August 2004). The calibration in all but one AATS-14 channel changed by less than 0.6% between pre-mission and in-mission calibrations; the calibration for the 499 nm channel, which

is most relevant to this study, changed by 0.4%. The resulting uncertainties in the derived AOD at 499 nm presented in this paper, including uncertainties due to imperfect tracking, calibration, Rayleigh and absorbing gas subtraction, and airmass factor calculation were in the range of 0.002 to 0.006.

3 Derivation of aerosol radiative forcing efficiency

3.1 Methodology

The basic idea for determining the direct instantaneous aerosol radiative forcing efficiency, E_i, from combined airborne AOD and irradiance measurements is to find the slope of the regression line of the spectral irradiance against midvisible AOD. To illustrate our methodology, Figure 1 shows the time traces of aerosol optical depth at 499 nm and numerically integrated broadband net (downwelling minus upwelling) irradiance between 350 and 700 nm (hereafter referred to as "visible broadband"), $F_{net}(350\text{-}700\ nm)$ for a case study on July 21, 2004. The increase in AOD by about 0.13 is accompanied by a decrease in net visible broadband irradiance of more than 15 W m^{-2}. To filter out fluctuations in the SSFR data caused by aircraft pitch and roll, the SSFR observations were screened to allow only those data points for which the cosine of the solar zenith angle with respect to the sensor differed by less than 3% from the cosine of the solar zenith angle with respect to the leveled plane [*Pilewskie et al*., 2003]. The AOD and irradiance data are then binned into AOD intervals of 0.005 or 0.01 width depending on data density during the observation period for each case study. Figure 2a shows the plot of the binned visible broadband net irradiance shown in Figure 1 versus AOD at 499 nm. The slope of the linear least-square regression line to the data yields the instantaneous forcing efficiency, E_i, in units of W m^{-2}

per unit midvisible AOD. The same procedure used for the numerically integrated broadband irradiance in Figure 1 can be applied to the spectrally resolved SSFR irradiance data. The slope of the regression line then yields the spectral instantaneous forcing efficiency in units of W m^{-2} nm^{-1} per unit midvisible AOD. Figure 2b and 2c illustrate the regression plots of spectral net irradiance at 506 nm and 1604 nm respectively for the same case study. Note the difference in units by comparison to Figure 2a.

3.2 Correction for changes in the solar zenith angle

Even in the absence of aerosol effects on the net irradiance measurements shown in Figures 1 and 2, there would be a change in the measured net irradiance caused by the change in the solar zenith angle during the observation period. Hence, to isolate the aerosol-induced effect, a correction of the irradiance measurements for the change in solar zenith angle is required. In addition to the dashed-line regression of the actual measurements depicted as squares, Figures 2a-c also contain circles and corresponding solid regression lines, which represent the irradiance measurements after such a correction for the change in the solar zenith angle has been applied. To compute this correction we utilized simplified expressions for aerosol induced irradiance changes derived by *Russell et al*. [1997] and *Russell et al*. [1999], based on the 2-stream approximation. *Russell et al*. [1997] introduced an analytical expression for the change in the atmosphere-plus-surface albedo, ΔR, at the top of the aerosol layer and showed that their result agreed well with adding-doubling calculations over a wide range of conditions and aerosol properties. Specifically, here we use equation (1) of *Russell et al*. [1999]:

$$F\downarrow_S(\mu_0) = \frac{F\downarrow_{dir,TL}(\mu_0)T_L(\mu_0)}{1-(\overline{R_L}+\overline{T_L}^2\overline{R_A})R_S(\mu_0)} + \frac{F\downarrow_{diff,TL}(\mu_0)\overline{T_L}}{1-(\overline{R_L}+\overline{T_L}^2\overline{R_A})\overline{R_S}} \quad (1)$$

to estimate the change in the downwelling irradiance at the surface, $F\downarrow_S$, caused by a change in the solar zenith angle during the observation period for each case study. In equation (1), $F\downarrow_{dir,TL}$ and $F\downarrow_{diff,TL}$ are the downwelling direct and diffuse irradiance at the top of the aerosol layer, respectively; T_L is the transmission of the aerosol layer, R_S is the surface albedo, R_L and R_A are the reflectivity of the aerosol layer and of the atmosphere above the aerosol layer, respectively; μ_0 is the cosine of the solar zenith angle, and overbars designate quantities for isotropic incident radiation (i.e., averaged over μ_0). Values for T and R as functions of AOD were computed using expressions derived by *Coakley and Chylek* [1975], while the diffuse and direct incident irradiance were computed using SBDART [*Ricchiazzi et al*., 1998] for a mid-latitude summer atmosphere model. The computations were carried out assuming that the aerosol layer has a geometric thickness of 3km, that the aerosol microphysical properties (asymmetry parameter and single scattering albedo) did not change during the observation period, and that no Rayleigh scattering or gaseous absorption occurred within the aerosol layer. To convert the calculations of surface irradiance to net irradiance we used the spectrally constant expression for the surface albedo as a function of solar zenith angle given by *Taylor et al.* [1996]. The magnitude of the corrections to the irradiance measurements thus derived can be seen as the difference in the squares and circles in the regression plots shown in Figures 2a-c. For example, for the integrated broadband visible net flux shown in Figure 2a, the maximum μ_0-correction applied to the irradiance measurement at an AOD of 0.46 is about 3.5 W m^{-2}. The aerosol effect over the entire

time period on the other hand is about 15 W m^{-2}, which means that the aerosol effect for this case study is a factor of four larger than the effect of the changing solar zenith angle.

3.3 Results for all 10 suitable case studies

In INTEX/ITCT, flying at the J31 minimum flight altitude of ~80 m ASL, we observed a total of 14 horizontal AOD gradients, with 10 gradients well suited for our analysis because of the small changes in solar zenith angle during the gradient measurements. More than half of the AOD changes $\Delta\tau$ (at wavelength 499 nm) were greater than 0.1 and extended over distances less than 40 km. Table 1 summarizes observational conditions and results of the 14 gradient cases, including the 10 cases deemed suitable for analysis. The fourth column shows the ratio of the change in μ_0 to the change in midvisible AOD. Because the four discarded cases would have required a larger μ_0-correction of the net irradiance than was measured due to the aerosol effect, we conclude that the conditions (1) $\Delta\tau>0.05$ and (2) $\Delta\mu_0/\Delta\tau\ll 1$ are necessary conditions for the successful application of the gradient method presented here. The four cases (#1, #6, #13 and #14) in Table 1 that did not fulfill the conditions above are not considered further in this paper. As an additional selection criterion, Table 1, column 5 contains the R^2-statistics of a univariate regression (with AOD as the regressor) and a bivariate regression (with AOD and μ_0 as regressors) of the visible broadband irradiance against midvisible AOD. Here, R^2 is a measure of the explained variability in the irradiance data due to the regressor(s). It can be seen that in all but one of the 10 cases that fulfill conditions (1) and (2) above, the explained variability does not increase in the bivariate regression, indicating that in those cases, changes in AOD are sufficient to explain the measured changes in net irradiance.

Figures 3a and 3b show the derived instantaneous spectral net forcing efficiencies, E_i, at 506 and 1604 nm for all 10 case studies described in Table 1. Figures 3c and 3d show the derived broadband net forcing efficiencies for the same cases studies for the spectral range of 350 to 1670 and 350 to 700 nm respectively. Within the 10 case studies we found a high variability in the derived instantaneous aerosol forcing efficiencies. For the broadband visible wavelength range (350-700nm), we derived a mean instantaneous forcing efficiency of -79.6Wm^{-2} and a standard deviation of 21.8Wm^{-2}(27%). The mean instantaneous forcing efficiency for the visible plus near-IR wavelength range (350-1670nm) was -135.3Wm^{-2} with a standard deviation of 36.0Wm^{-2}(27%). The similarity in derived efficiencies for cases flown back to back (e.g., case 4 and 5) supports the validity of our method.

Figures 3c and 3d are plotted at the same scales to illustrate the very different effects on the various spectral ranges. In comparing Figures 3a and 3b, it is obvious that the absolute forcing efficiency is much larger for the visible channel than it is for the near-IR channel. This is because aerosols scatter radiation more effectively in the visible portion of the spectrum compared to the near-infrared and also because there is a greater amount of solar radiation available in the mid-visible. To remove the variability due to the spectral distribution of solar irradiance we introduce "relative forcing efficiency", which is the instantaneous absolute forcing efficiency shown in Figure 3 normalized by the incident, downwelling irradiance, $e_i = E_i / F_i^{\downarrow}$. Figure 4 shows the relative forcing efficiency, e_i, for the same wavelengths and case studies given in Figure 3. Comparing Figure 4a and 4b, we note that the aerosols present during the 10 INTEX/ITCT case studies presented here reduce the net irradiance at the visible wavelength (506 nm), by between 10 and 25% of the downwelling, but they have a much smaller relative effect on the near-IR

irradiance (1604 nm). The fact that 3 of the 10 cases studied show physically implausible positive forcing efficiencies at 1604 nm illustrates the uncertainty of our method for the small absolute irradiances at that wavelength. To calculate the uncertainty in forcing efficiency we used standard expressions for the uncertainties in regression line parameters (cf., *Bevington and Robinson*, 1992). Since the forcing efficiency is derived as the slope of the regression line of net irradiance versus AOD, the uncertainty in the forcing efficiency is simply the uncertainty of the slope of the regression line. Uncertainties thus derived are shown as error bars in Figures 3 and 4. We see that the uncertainties for two of the three cases with positive forcing efficiencies at 1604 nm reach into the physically plausible negative forcing region.

In comparing Figures 4c and 4d, we find that the relative forcing efficiencies for the two broadband regions, 350-700 and 350-1670 nm are similar. The range of Ångstrom parameters (i.e., the negative of the slope of the line fit between $\ln(\lambda)$ and $\ln(\tau)$, not shown here) for the 10 case studies was well-confined in the range between 1.2 and 1.8 and generally did not change during the measurements for each case, supporting the implicit assumption that changes in aerosol optical depth were due to changes in concentration rather than changes in size or composition. However, for a small number of cases, there was a change in the AATS-derived measurements of columnar water vapor coincident with the aerosol gradient. In these cases, the derived aerosol broadband forcing efficiencies between 350 and 1670 nm will be affected, because of water vapor absorption at wavelengths greater than 700 nm. The visible (350 – 700 nm) broadband forcing efficiencies are much less affected by changes in columnar water vapor during the aerosol gradient observations.

As an extension of Figure 4, Figure 5 shows the instantaneous spectral relative forcing efficiency, e_i, for the five SSFR channels at 380, 506, 762, 1052 and 1604 nm. These channels were chosen because they are largely unaffected by water vapor absorption and hence changes in columnar water vapor during the aerosol gradient observations. Figure 6 indicates that the relative forcing efficiencies decrease monotonically from the near-UV to the near-IR for all 10 cases, with some case studies showing an almost linear trend in the wavelength range covered here. This finding could have an important implication for experimental assessments of aerosol radiative forcing of climate in the future. The near-linear relationship suggests that a rather simple parameterization scheme could be employed to model the surface radiative forcing of aerosol layers under varying levels of incident solar radiation.

3.4 Estimation of broadband visible aerosol single scattering albedos

To answer the question what range of aerosol single scattering albedos may be most consistent with the measured irradiance and AOD gradients, we now describe a simple estimation scheme for the broadband visible aerosol single scattering albedos, ϖ_o. Specifically, we use the ratio of regressed net irradiance at the smallest AOD to the regressed net irradiance at the highest AOD in the regression plots of net irradiance versus mid-visible AOD (hereafter referred to as Q_{meas}). For each case study, we use equation (1) above to compute $Q(\varpi_o)$ as a function of aerosol single scattering albedo and compare our computations to the value of Q_{meas}. The value of ϖ_o for which the difference between $Q(\varpi_o)$ and Q_{meas} is smallest is thus the best-estimate single scattering albedo. To minimize computational effort, we investigate only the broadband visible spectral region, seeking the best-fit aerosol single scattering albedo assumed to be constant between 350

and 700 nm. In our computations of the theoretical flux gradients, we used the Ångstrom parameters derived from the AATS AOD spectra to determine the spectral AOD between 350 and 700 nm and we assumed a spectrally constant asymmetry parameter of 0.7. Column 8 of Table 1 shows the best-fit single scattering albedos thus derived. To estimate the uncertainty in ϖ_o we used standard equations (cf., *Bevington and Robinson*, 1992) to propagate the uncertainties in the regression line fit parameters into Q_{meas}. The range of single scattering albedos for which the computations of $Q(\varpi_o)$ are within the range of uncertainties of Q_{meas} are reported as the uncertainty in aerosol single scattering albedo in column 8 of Table 1. Hence, the uncertainty in single scattering albedo is a direct reflection of the quality of the regression line fit of net irradiance versus mid-visible AOD.

Assuming an asymmetry parameter of 0.65 or 0.75 in our computations of $Q(\varpi_o)$ changed our estimated single scattering albedos by less than 0.02. We note that the generally lower estimates of aerosol single scattering albedo of about 0.9 on July 21 and 23, 2004, are consistent with trajectory analyses, which showed the INTEX/ITCT study area affected by long range transport of biomass burning aerosol from Alaskan forest fires during that time period.

3.5 Translation of instantaneous forcing efficiencies to diurnally-averaged values and comparisons with previous studies

In addition to using equation (1) above to correct for the changes in net irradiance caused by changes in μ_0 during the observation period, we further employed the equation to calculate the diurnal cycle of the aerosol radiative forcing. This procedure is necessary to translate the derived

instantaneous radiative forcing efficiency, E_i, to a diurnally averaged forcing efficiency, E_{24h}, using:

$$E_{24h} = \int_{24h} E_i dt \Big/ 24h \tag{2}$$

Equation (2) holds for both the forcing efficiency as shown, and also for the absolute forcing, $\Delta_{24h}F$. Figure 6a shows the diurnal variation in the net visible broadband aerosol radiative forcing, $\Delta_i F$, for the 10 cases studies discussed in the previous section. For each of the 10 case studies, there are three curves corresponding to pairs of aerosol single scattering albedo and asymmetry parameter of 0.9/0.65, 0.95/0.7 and 1.0/0.75, respectively. Aerosol optical depths were assumed to be equal to the mean values obtained during the gradient flights described above. After integration over the diurnal cycle the curves in Figure 6a can be translated into a conversion of the instantaneous radiative forcing to the diurnal average. This ratio is shown in Figure 6b as a function of the cosine of the solar zenith angle, μ_0. The thick black lines in Figure 6b denote the mean (solid) and standard deviation (dashed) of the 30 curves in Figure 6a respectively. It can be seen that despite the large absolute range of instantaneous forcings, the ratios of instantaneous forcings to 24-h averages are rather well confined. For example, at a μ_0 of 0.8 the mean and standard deviation of the ratio is about 1.7 and 0.15 respectively. An application of the mean conversion curve given in Figure 6b to the instantaneous forcings and forcing efficiencies in Table 1 yields the diurnally averaged forcing efficiencies of -45.8±13.1Wm^{-2} (mean±std, given in column 9 of Table 1) for the visible, and -82.9±23.1Wm^{-2} (mean±std) for the visible plus near-IR wavelength range (not shown in Table 1), respectively. Because most case studies occurred at comparable solar zenith angles (μ_0~0.85), the standard

deviation of the 24-h average forcings is similar to the standard deviation of the instantaneous forcings.

Comparing our results with previous, radiometrically-determined estimates of direct aerosol radiative forcing in the peer-reviewed literature, we note that the most readily reported quantity is the diurnally averaged direct radiative forcing efficiency, E_{24h}, at the surface. *Kim et al*. [2005] report values for the broadband range of 300 - 4000 nm under dust and no-dust conditions in East Asia. Their values for E_{24h} range from -55 to -104 W m^{-2} per unit optical depth, the latter under dust conditions. Hence, their results bracket our 10-case average value of -82.9±23.1 (mean±std) W m^{-2}. *Meywerk and Ramanathan* [1999] report a noon-time forcing efficiency that translates to a diurnal average value of about -48 W m^{-2} per unit optical depth for the wavelength range of 400 to 700 nm during the INDOEX campaign, which is close to our value of 45.8 W m^{-2}, but appears small considering the high aerosol absorption measurements encountered during INDOEX. Finally, *Bush and Valero* [2002, 2003] report values from ground-based radiometer measurements in INDOEX and ACE-Asia. They retrieve mission-average values for the visible broadband E_{24h} *(400-700 nm)* of 38.5±4.0 and 42.2±4.8 W m^{-2} per unit optical depth for INDOEX and ACE-Asia respectively. For the entire solar spectrum (300-3810 nm) they obtain E_{24h} of 72.2±5.5 and 73.0±9.6 W m^{-2} per unit optical depth for the two experiments respectively. These values are lower than the values reported here but they are within one standard deviation of our results.

4 Discussion

As part of the INTEX/ ITCT field studies, we present measurements from aboard a Sky Research Jetstream 31 (J31) aircraft. The combination of coincident and simultaneous AATS and SSFR measurements was used to determine the change in net irradiance per change in aerosol optical depth (i.e., the direct aerosol radiative forcing efficiency [W m^{-2}]), a technique referred to as the aerosol gradient method. Unlike ground-based measurements of direct aerosol radiative forcing which rely upon the advection of various air masses over a measurement site during an extended period of time, the aerosol gradient method has the advantage of being quasi-instantaneous. The airborne method minimizes the risk of changes in thermodynamics or aerosol microphysics during the observations.

We observed a total of 14 horizontal AOD gradients, with 10 gradients well suited for our analysis because of the small changes in solar zenith angle during the gradient measurements. More than half the cases had AOD changes $\Delta\tau$(499 nm) grater than 0.1 and extended over distances less than 40 km. Within the 10 case studies we found a high variability in the derived instantaneous aerosol forcing efficiencies (forcing per unit optical depth) for the visible wavelength range (350-700nm), with a mean of -79.6 W m^{-2} and a standard deviation of 21.8 W m^{-2}(27%). The mean instantaneous forcing efficiency for the visible plus near-IR wavelength range (350-1670nm) was derived to be -135.3 W m^{-2} with a standard deviation of 36.0 W m^{-2}(27%). An analytical conversion of the instantaneous forcing efficiencies to 24h-average values yielded -45.8±13.1 W m^{-2} (mean±std) for the visible and -82.9±23.1 W m^{-2} (mean±std) for the visible plus near-IR wavelength range, respectively. The large spread in the individual cases is probably caused by the wide range of aerosol types and aerosol absorption values encountered

during INTEX-B. We show that our broadband forcing efficiency results are consistent with previously reported values from ground-based observations during ACE-Asia and INDOEX. The spectral dependence of the relative forcing efficiency, i.e., the forcing efficiency normalized to incident downwelling irradiance, was shown to be monotonically decreasing from the near-UV to the near-IR, with some cases exhibiting a near-linear spectral dependence. Estimates of the aerosol single scattering albedo obtained from matching 2-stream radiative transfer calculations with measured gradients in aerosol optical depth and net irradiance were consistent with independent trajectory analyses and satellite imagery, which showed the influence of biomass burning aerosol from Alaskan forest fires during the first half of the INTEX/ITCT experiment. In conclusion, airborne measurements of spectral direct aerosol radiative forcing efficiency have been proven to be a powerful tool in determining the regional effects of aerosols on climate. The forcing efficiencies derived here are likely of high value for improving and testing regional climate models and should therefore be carried out more frequently in different geographical locations.

Acknowledgements

Funding for the J31 aircraft modifications through the NASA RSP (Radiation Science Program), TCP (Tropospheric Chemistry Program) and SSP (Suborbital Science Program), and for ICARTT measurements and data analysis through NOAA ACCP (Atmospheric Climate/Chemistry Program) are gratefully acknowledged.

References

Bevington, P.R., and D.K. Robinson, Data Reduction and Error Analysis for the Physical Sciences, 2nd ed., McGraw-Hill, 1992.

Bush, B.C., and F. P. J. Valero, Spectral aerosol radiative forcing at the surface during the Indian Ocean Experiment (INDOEX), *J. Geophys. Res.*, 107(D19), 8003, doi:10.1029/2000JD000020, 2002.

Bush, B.C., and F. P. J. Valero, Surface aerosol radiative forcing at Gosan during the ACE-Asia campaign, *J. Geophys. Res.*, 108(D23), 8660, doi:10.1029/2002JD003233, 2003.

Coakley, J., and P. Chylek, The two-stream approximation in radiative transfer: Including the angle of incident radiation, *J. Atmos. Sci.*, *32*, 409-418, 1975.

Coakley, J. A., Jr., W. R. Tahnk, A. Jayaraman, P. K. Quinn, C. Devaux, and D. Tanré, Aerosol optical depths and direct radiative forcing for INDOEX derived from AVHRR: Theory, J. Geophys. Res., 107(D19), 8009, doi:10.1029/2000JD000182, 2002.

Fiebig, M., A. Petzold, U. Wandinger, M. Wendisch, C. Kiemle, A. Stifter, M. Ebert, T. Rother, and U. Leiterer, Optical closure for an aerosol column: Method, accuracy, and inferable properties applied to a biomass-burning aerosol and its radiative forcing, *J. Geophys. Res.*, 107(D21), 8130, doi:10.1029/2000JD000192, 2002.

Hansen, J., M. Sato, and R. Ruedy, Radiative forcing and climate response, *J. Geophys. Res., 102*, 6831-6864, 1997.

Hignett, P., J. P. Taylor, P. N. Francis, and M. D. Glew, Comparison of observed and modeled direct aerosol forcing during TARFOX, *J. Geophys. Res.*, 104(D2), 2279–2288, 1999.

Kim, D.-H., B. J. Sohn, T. Nakajima, and T. Takamura, Aerosol radiative forcing over east Asia determined from ground-based solar radiation measurements, J. Geophys. Res., 110, D10S22, doi:10.1029/2004JD004678, 2005.

Meywerk, J., and V. Ramanathan, Influence of anthropogenic aerosols on the total and spectral irradiance at the sea surface during the Indian Ocean Experiment (INDOEX) 1999, *J. Geophys. Res.*, 107(D19), 8018, doi:10.1029/2000JD000022, 2002.

Pilewskie, P., J. Pommier, R. Bergstrom, W. Gore, S. Howard, M. Rabbette, B. Schmid, P. V. Hobbs, and S. C. Tsay, Solar spectral radiative forcing during the Southern African Regional Science Initiative, J. Geophys. Res., 108(D13), 8486, doi:10.1029/2002JD002411, 2003.

Pope, S.K., and F.P.J. Valero, Aerosol Forcing from INDOEX and ACE-Asia Aircraft Measurements, Geophysical Research Abstracts, Vol. 6, 06103, 2004.

Redemann, J., R. P. Turco, K. N. Liou, P. V. Hobbs, W. S. Hartley, R. W. Bergstrom, E. V. Browell, and P. B. Russell, Case studies of the vertical structure of the direct shortwave aerosol radiative forcing during TARFOX, *J. Geophys. Res.*, 105(D8), 9971–9980, 2000.

Redemann, J., B. Schmid , J. A. Eilers, R.A. Kahn, R. C. Levy, P. B. Russell, J. M. Livingston, P. V. Hobbs, W. L. Smith Jr., B. N. Holben, Suborbital measurements of spectral aerosol optical depth and its variability at sub-satellite grid scales in support of CLAMS, 2001, *J. Atmos. Sci.* , doi:10.1175/JAS3387.1, Vol. 62, No. 4, pp. 993-1007, 2005.

Ricchiazzi, P., S. Yang, C. Gautier, and D. Sowie, SBDART: A research and teaching software tool for plane-parallel radiative transfer in the Earth's atmosphere, BAMS, 79 (10), 2101-2114, 1998.

Russell, P. B., S. Kinne, and R. Bergstrom, Aerosol climate effects: Local radiative forcing and column closure experiments, *J. Geophys. Res., 102*, 9397-9407, 1997.

Russell, P. B., J. M. Livingston, P. Hignett, S. Kinne, J. Wong, and P. V. Hobbs, Aerosol-induced radiative flux changes off the United States Mid-Atlantic coast: Comparison of values calculated from sunphotometer and in situ data with those measured by airborne pyranometer, *J. Geophys. Res., 104*, 2289-2307, 1999.

Russell, P. B., and J. Heintzenberg, An Overview of the ACE 2 Clear Sky Column Closure Experiment (CLEARCOLUMN), *Tellus* B 52, 463-483, 2000.

Schmid, B., and C. Wehrli, Comparison of Sun Photometer Calibration by Langley Technique and Standard Lamp. *Appl. Opt., 34*(21), 4500-4512, 1995.

Schmid, B., C. Mätzler, A. Heimo, and N. Kämpfer, Retrieval of Optical Depth and Size Distribution of Tropospheric and Stratospheric Aerosols by Means of Sun Photometry. *IEEE Geosci. Remote. Sens*., 35(1), 172-182, 1997.

Schmid B., J.J. Michalsky, D.W. Slater, J.C. Barnard, R.N. Halthore, J.C. Liljegren, B.N. Holben, T.F. Eck, J.M. Livingston, P.B. Russell, T. Ingold, and I. Slutsker. Comparison of columnar water-vapor measurements from solar transmittance methods. *Applied Optics,* Vol. 40, No. 12, 1886-1896, 2001.

Taylor, J.P., J.M. Edwards, M.D. Glew, P Hignett and A. Slingo, Studies with a flexible new radiation code. II: Comparisons with aircraft short-wave observations, *Q.J.Roy.Met.Soc*., 122, pp. 839-861, 1996.

Zhang, J., S.A. Christopher, L.A. Remer and Y.J. Kaufman, Shortwave Aerosol Cloud-Free Radiative Forcing from Terra, II: Global and Seasonal Distributions, *J. Geophys. Res.*, D10, S24, doi:10.1029/2004jd005009, 2005.

Figure captions

Figure 1. Time series of numerically integrated broadband visible (350-700nm) net irradiance (blue) and midvisible (499 nm) aerosol optical depth (red) for INTEX/ITCT case study 2, July 21, 2004.

Figure 2. a) Regression plot of binned broadband visible net irradiance shown in Figure 1 versus midvisible aerosol optical depth. The slope of the regression line yields the instantaneous aerosol radiative forcing efficiency, $\Delta_i E(350\text{-}700\ nm)$. b) Like a), but for the spectral net irradiance at 506 nm. c) Like b), but for the spectral net irradiance at 1604 nm. Note the difference in units between a) and b) or c).

Figure 3. a) Derived instantaneous spectral net aerosol radiative forcing efficiency, $\Delta_i E$, for the SSFR channel at 506 nm for the 10 case studies listed in Table 1. b) Like a), but for the SSFR channel at 1604 nm. c) Like a), but numerically integrated over the spectral range between 350 and 1670 nm. d) Like c), but numerically integrated over the spectral range between 350 and 700 nm. The squares represent the forcing efficiencies without a correction for the changing solar zenith angle.

Figure 4. a) Derived instantaneous spectral net relative aerosol radiative forcing efficiency, $\delta_i E$, (normalized to downwelling irradiance) for the SSFR channel at 506 nm for the 10 case studies listed in Table 1. b) Like a), but for the SSFR channel at 1604 nm. c) Like a), but numerically

integrated over the spectral range between 350 and 1670 nm. d) Like c), but numerically integrated over the spectral range between 350 and 700 nm. The squares represent the relative forcing efficiencies without a correction for the changing solar zenith angle.

Figure 5. Derived instantaneous spectral net relative aerosol radiative forcing efficiency, $\delta_i E$, as a function of wavelength for the 10 case studies listed in Table 1.

Figure 6. a) Diurnal variation of the instantaneous aerosol radiative forcing, $\Delta_i F(350\text{-}700\ nm)$, for the 10 case studies listed in Table 1 for 3 pairs of aerosol single scattering albedo and asymmetry parameters (0.9/0.65, 0.95/0.7, 1.0/0.75). b) Ratio of instantaneous to diurnally averaged aerosol radiative forcing for the set of curves shown in a). The solid and dashed black line represents the mean and the standard deviation of the set of curves in a), respectively.

Table 1. Summary of gradient cases used in this paper. All irradiance results are given for the wavelength range of 350 to 700 nm. All optical depth results are reported at 499 nm. The mean absolute forcings, $\Delta_i F$, are calculated by multiplying the forcing efficiencies, E_i, by the mean aerosol optical depth during each of the gradient measurements.

#	Date in 2004	$\Delta\tau$, distance [km]	$\frac{\Delta\mu_0}{\Delta\tau}$	$R^2(\tau)$, $R^2(\tau,\mu_0)$	E_i unc. [W m^{-2}]	$\Delta_i F$ unc. [W m^{-2}]	ϖ_o unc.	E_{24h} unc. [W m^{-2}]	$\Delta_{24h} F$ unc. [W m^{-2}]
1	7/17	↓ 0.016 (25.2%) 15.3km	0.31	0.54 1.00					
2	7/21	↑ 0.134 (41.5%) 30.2km	0.04	0.92 0.92	-111.1 7.8	-43.4 3.0	0.89 0.09	-64.2 7.6	-25.1 3.0
3	7/22	↓ 0.069 (14.7%) 13.2km	0.05	0.56 0.56	-73.2 35.3	-36.9 17.8	0.96 >0.1	-42.7 21.1	-21.5 10.6
4	7/23	↑ 0.201 (40.0%) 22.5km	0.02	0.88 0.88	-106.2 7.2	-64.1 4.4	0.89 0.09	-62.1 7.7	-37.5 4.6
5	7/23	↓ 0.070 (11.0%) 8.0km	0.02	0.65 0.88	-109.9 27.1	-73.4 18.1	0.88 >0.1	-64.2 17.1	-42.9 11.5
6	7/23	↑ 0.039 (5.1%) 6.8km	0.03	0.92 0.95					
7	7/29	↓ 0.143 (38.1%) 18.7km	0.02	0.93 0.95	-73.1 6.1	-32.6 2.7	0.96 0.06	-42.5 5.5	-19.0 2.5
8	7/29	↑ 0.378 (91.3%) 28.4km	0.02	0.78 0.81	-55.3 3.9	-33.4 2.3	0.99 0.02	-32.2 4.0	-19.4 2.4
9	7/29	↓ 0.177 (35.1%) 6.5km	0.00	0.89 0.89	-65.6 4.1	-38.8 2.4	0.97 0.04	-38.5 4.7	-22.8 2.8
10	8/02	↓ 0.245 (124.6%) 42.9km	0.03	0.97 0.97	-80.9 2.4	-25.8 0.8	0.96 0.02	-46.5 4.5	-14.8 1.4
11	8/02	↑ 0.219 (111.8%) 44.7km	0.05	0.78 0.85	-58.6 3.6	-17.9 1.1	0.98 0.02	-34.1 4.0	-10.4 1.2
12	8/03	↑ 0.095 (25.5%) 33.1km	0.23	0.86 0.86	-61.4 21.3	-25.7 8.9	1.00 >0.1	-31.3 10.9	-13.1 4.5
13	8/07	↓ 0.02 (27.6%) 64.4km	1.00	0.67 1.00					
14	8/08	↑ 0.036 (66.5%) 108.3km	0.58	0.88 0.99					
				mean =	-79.5	-39.2	0.95	-45.8	-22.6
				std =	21.8	17.3	0.04	13.1	10.3
				rel_std =	27.4%	44.2%	4.5%	28.6%	45.6%

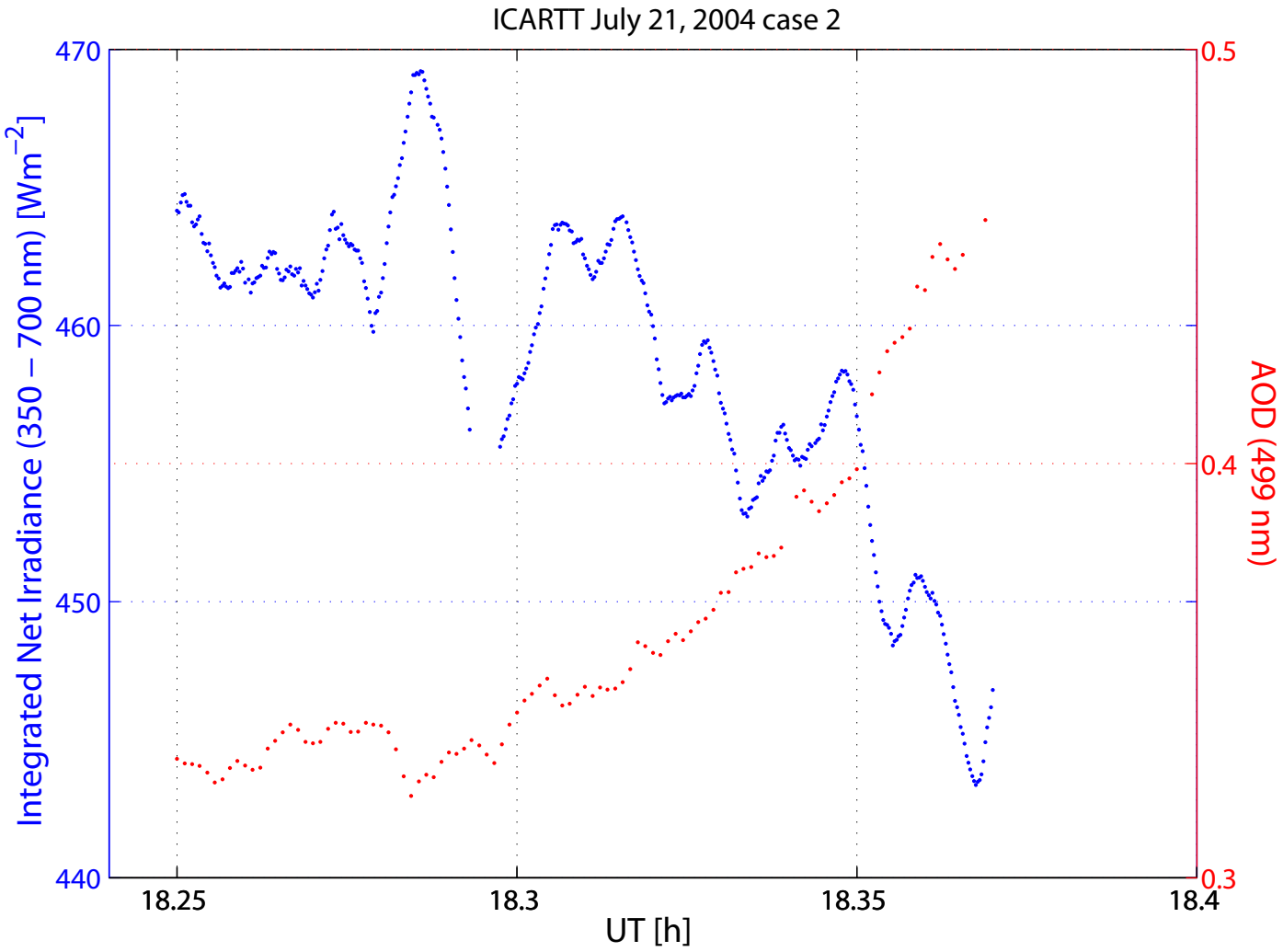
ICARTT July 21, 2004 case 2
470
460
450
440
0.5
0.4
0.3
18.25
18.3
18.35
18.4
UT [h]
Integrated Net Irradiance (350 – 700 nm) [Wm^{-2}]
AOD (499 nm)

Figure 1.

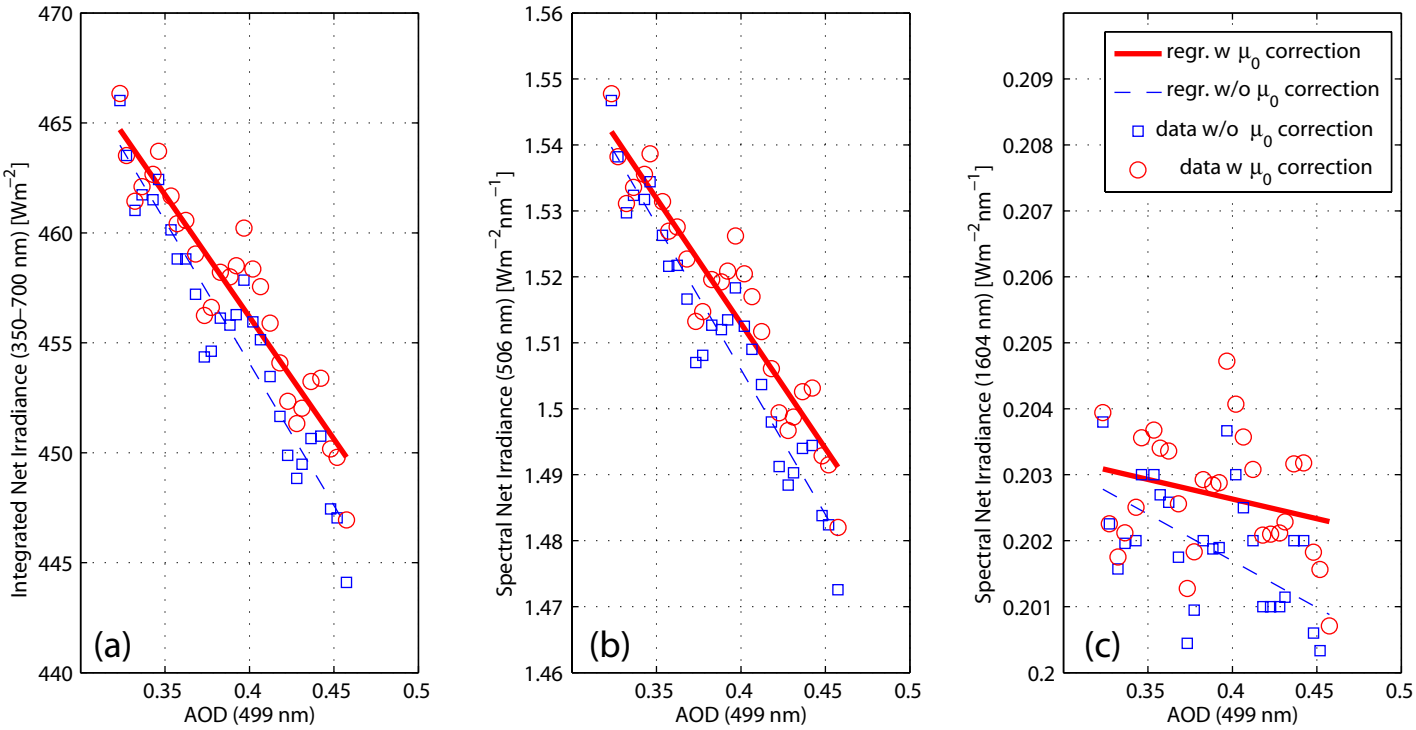
470
465
460
455
450
445
440
Integrated Net Irradiance (350–700 nm) [Wm^{-2}]
(a)
0.35
0.4
0.45
0.5
AOD (499 nm)
1.56
1.55
1.54
1.53
1.52
1.51
1.5
1.49
1.48
1.47
1.46
Spectral Net Irradiance (506 nm) [Wm^{-2}nm^{-1}]
(b)
0.35
0.4
0.45
0.5
AOD (499 nm)
0.209
0.208
0.207
0.206
0.205
0.204
0.203
0.202
0.201
0.2
Spectral Net Irradiance (1604 nm) [Wm^{-2}nm^{-1}]
(c)
0.35
0.4
0.45
0.5
AOD (499 nm)
regr. w μ_0 correction
regr. w/o μ_0 correction
data w/o μ_0 correction
data w μ_0 correction

Figure 2.

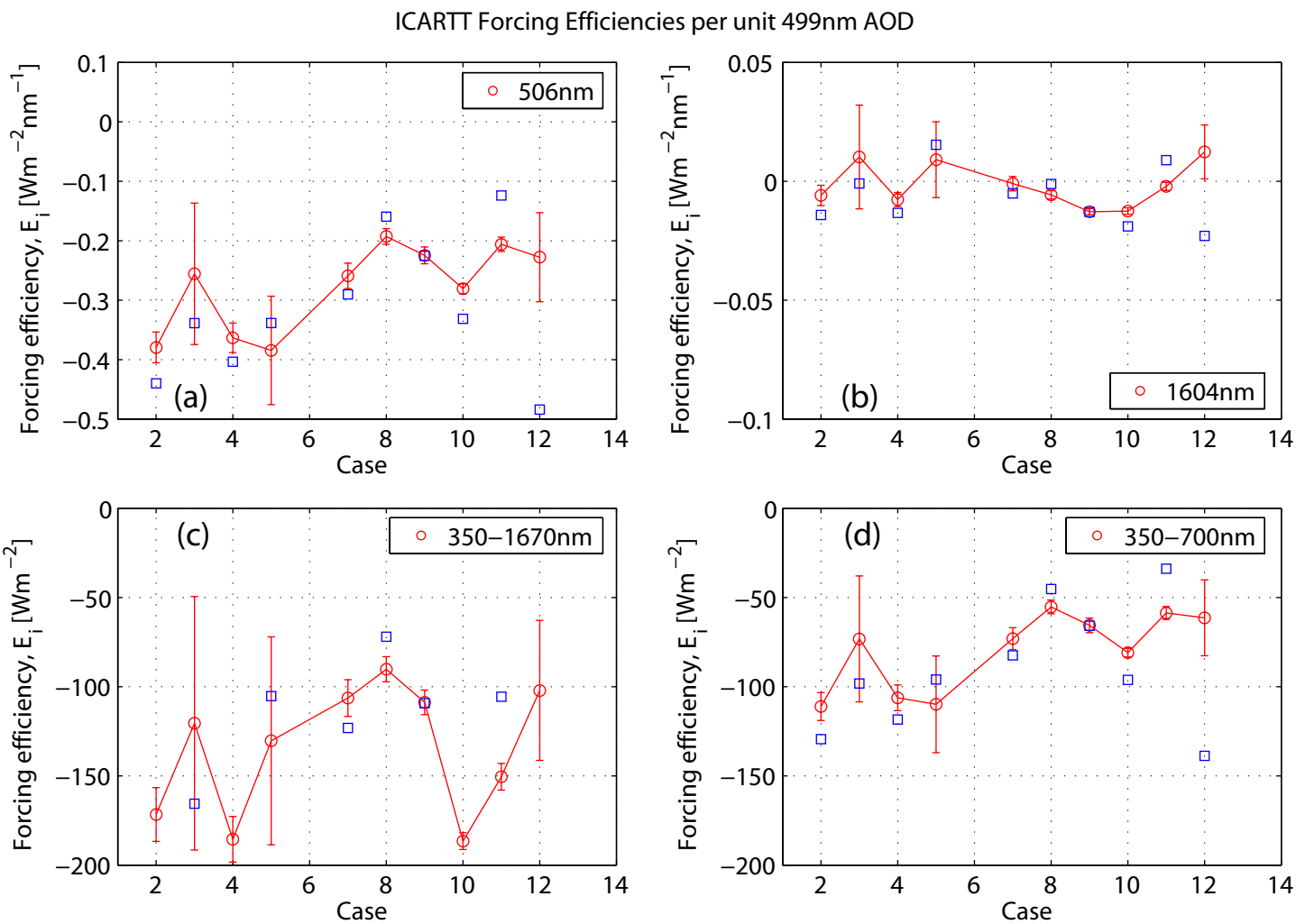
ICARTT Forcing Efficiencies per unit 499nm AOD
(a)
506nm
(b)
1604nm
(c)
350−1670nm
(d)
350−700nm
Forcing efficiency, E_i [Wm^−2nm^−1]
Forcing efficiency, E_i [Wm^−2]
Case

Figure 3.

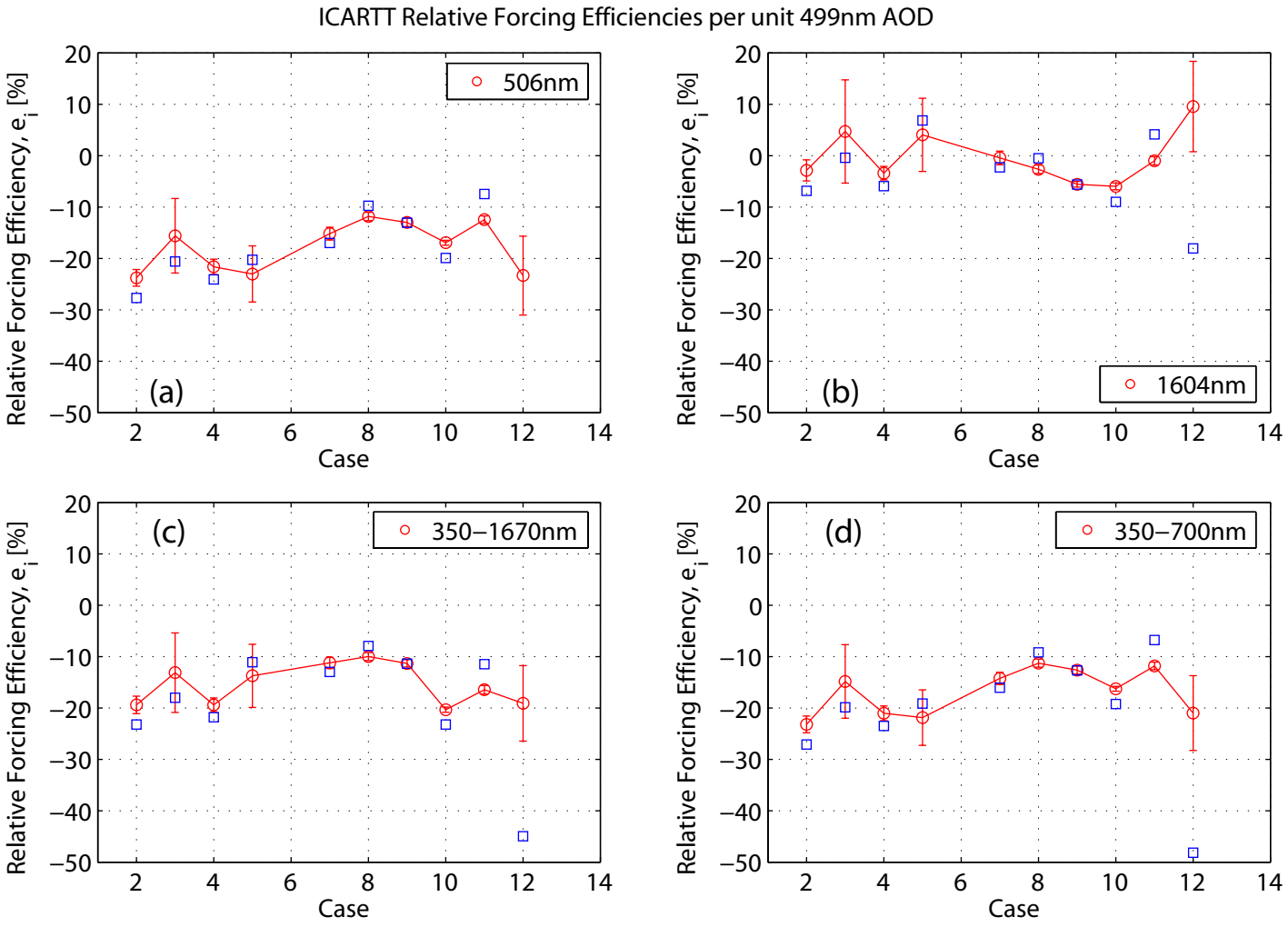
ICARTT Relative Forcing Efficiencies per unit 499nm AOD
Relative Forcing Efficiency, e_i [%]
Case
(a)
506nm
(b)
1604nm
(c)
350−1670nm
(d)
350−700nm

Figure 4.

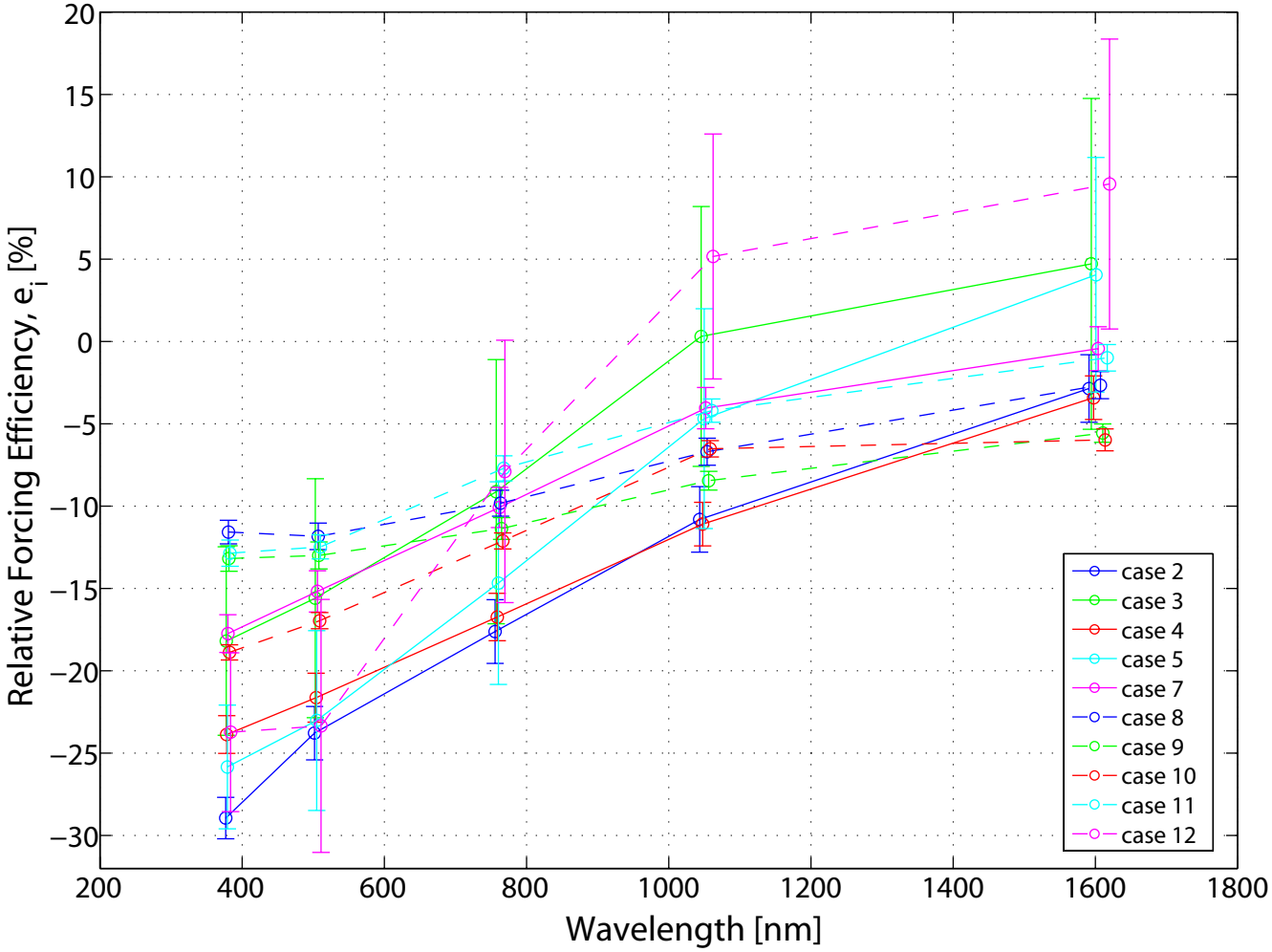
Relative Forcing Efficiency, e_i [%]
Wavelength [nm]
20
15
10
5
0
−5
−10
−15
−20
−25
−30
200
400
600
800
1000
1200
1400
1600
1800
case 2
case 3
case 4
case 5
case 7
case 8
case 9
case 10
case 11
case 12

Figure 5.

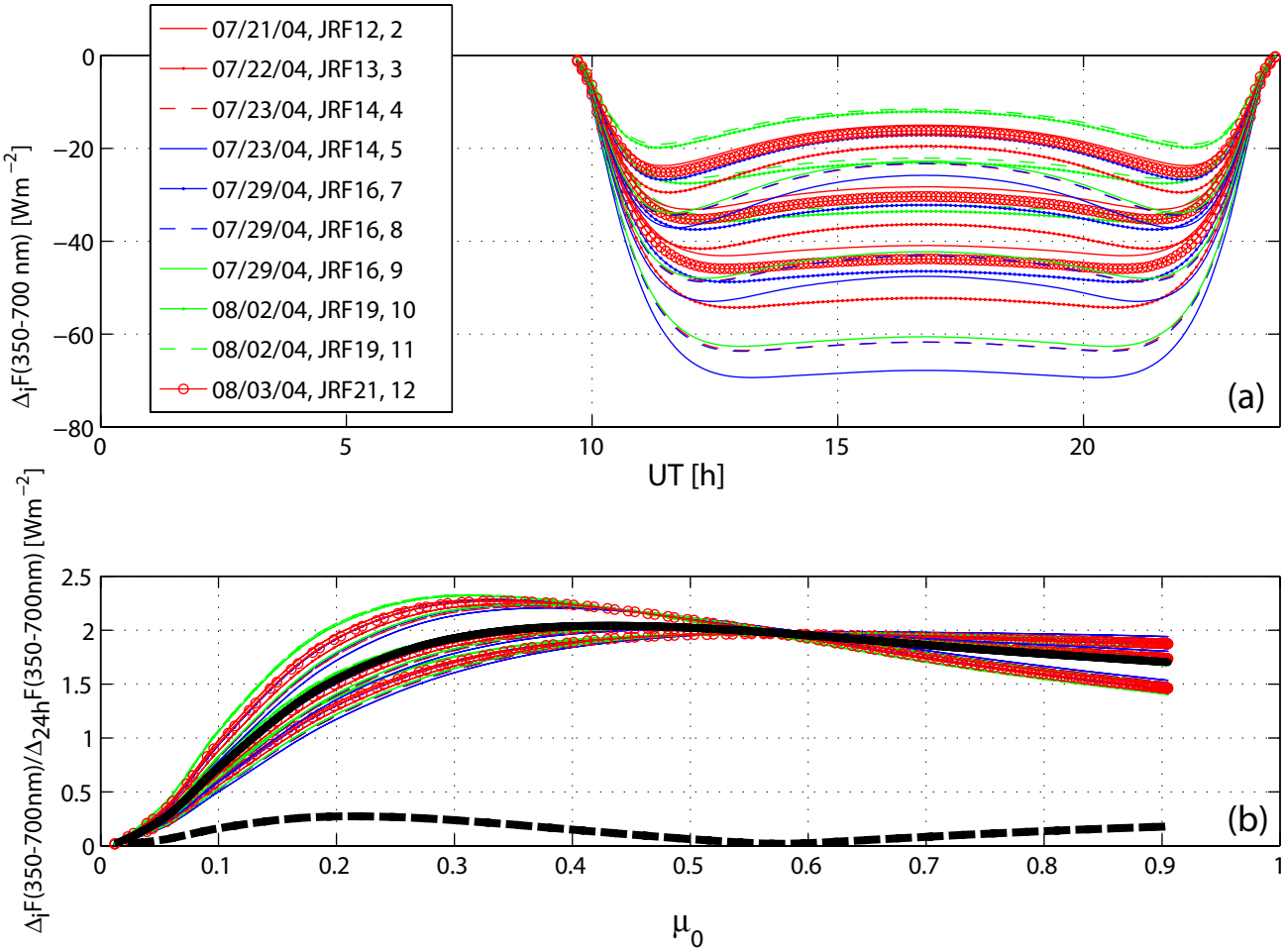
07/21/04, JRF12, 2
07/22/04, JRF13, 3
07/23/04, JRF14, 4
07/23/04, JRF14, 5
07/29/04, JRF16, 7
07/29/04, JRF16, 8
07/29/04, JRF16, 9
08/02/04, JRF19, 10
08/02/04, JRF19, 11
08/03/04, JRF21, 12
(a)
$\Delta_I F$(350-700 nm) [Wm^{-2}]
UT [h]
(b)
$\Delta_I F$(350-700nm)/$\Delta_{24h} F$(350-700nm) [Wm^{-2}]
μ_0

Figure 6.